ChemCommn RSCPublishing

COMMUNICATION

Electronic Supplementary Information:

Polypyrrole-polyoxometalate / reduced graphene oxide ternary nanohybrids for flexible, all-solid-state supercapacitors

Yuyun Chen,† Min Han,† Yujia Tang, Jianchun Bao, Shunli Li, Yaqian Lan,* and Zhihui Dai*

Jiangsu Key Laboratory of Biofunctional Materials, School of Chemistry and Materials Science, Nanjing Normal University, Nanjing 210023, P. R. China

E-mail: daizhihuii@njnu.edu.cn (Prof. Z. Dai); yqlan@njnu.edu.cn (Prof. Y. Lan)

Tel/Fax: +86-25-85891051

[†] M. Han and Y. Chen contribute equally to this work.

This information contains:

1. Experimental section

1.1 Reagents and materials

The natural graphite flakes, phosphomolybdic acid ($H_3PMo_{12}O_{40}$, *abbrev.* PMo_{12}), pyrrole (Py), $KMnO_4$, H_2O_2 , HCl (36 wt.%), H_2SO_4 (98 %), hydrazine hydrate (50 wt.%), ammonium persulfate (APS), cetyltrimethylammonium bromide (CTAB), and sodium dodecyl sulfate (SDS) were purchased from Sinopharm Chemical Reagent Co. Ltd. All those reagents were analytical grade and directly used without further purification. All aqueous solutions were prepared with deionized water. The acetylene black (ATB), poly-tetrafluoroethylene (PTFE) dispersion (60%), polyvinyl alcohol (PVA), and poly (ethylene terephthalate) (PET) pieces were purchased from Alfa Aesar.

1. 2 Synthesis of PPy-PMo_{12}/rGO ternary nanohybrids

In a typical synthesis procedure, graphene oxide (GO) nanosheets (NSs) are pre-synthesized by chemical oxidation/exfoliation of natural graphite flakes using the modified Hummers' method.[1] The obtained GO NSs are dispersed in de-ionized water by ultra-sonication to form a suspension with a concentration of 1 mg mL^{-1}. Next, 25 mL of the GO suspension and 300 mL of 4 mM PMo_{12} solution are added into a clean three-necked flask and mixed uniformly in a strong ultra-sonication bath. Subsequently, a pyrrole (Py) monomer solution produced by dispersing 434 μL of Py in 25 mL of de-ionized water, is slowly dropped into the above mixed GO-PMo_{12} suspension. With the addition of the Py monomer solution, the reaction system gradually turns from yellow-brown to deep blue and a black precipitate is generated after about 5 min. Finally, the reactor is transferred to an oil bath and allowed to react for 24 h at 60°C while vigorously stirring using a magnetic stirrer. After separation by centrifugation and washing with deionized water and anhydrous ethanol several times, black PPy-PMo_{12}/rGO ternary nanohybrids are obtained. The obtained nanohybrids are dried in a vacuum at 60°C for 24 h and used for subsequent characterization.

1.3 Synthesis of the PPy/rGO control sample

Before the synthesis, the PPy microsheets are firstly prepared according to a previously reported method with slight modifications.[2] The detailed procedures are as follows: 7.3 g of CTAB is dissolved in 120 mL of a 1 M HCl solution in an ice bath. Next, 13.7 g of APS is slowly added during magnetic stirring, which immediately turns the solution into pale-yellow. Subsequently, the reactor is transferred to an ultrasonic bath and sonicated for 4 h. After the reactor is cooled to 0 ~ 5 °C, 16.6 mL of pyrrole monomer is added into the reaction system and kept at that temperature for 24 h. With the initiation of the polymerization reaction, the pale-yellow solution immediately becomes black. The precipitates are collected by centrifugation, and washed with a large amount of dilute HCl solution and deionized water until the supernatant became colorless and neutral. After during in a vacuum at 60°C for 24 h, the PPy microsheets are obtained and used for synthesis of PPy/rGO control sample.

For synthesis of the PPy/rGO control sample, 50 mL of aqueous solution of PPy microsheets (0.05 g) and 50 mL of GO suspension (1 mg mL^{-1}) are mixed together in a clean 250 mL, three-necked flask while vigorously stirring using a magnetic stirrer. Then, a certain amount of hydrazine hydrate is immediately added into the reaction system. Finally, the reactor was heated to 90 °C and maintained at that temperature for 2 h. After naturally cooling the reactor to room temperature, the black solids are collected by centrifugation, and washed with deionized water for several times to remove the byproducts. The obtained black solids are dried in vacuum at 60°C for 24 h and used for further characterization.

1.4 Characterizations

The transmission electron microscopy (TEM) images are taken on a JEM-200CX instrument (Japan) at an accelerating voltage of 200 kV. The field-emission scanning electron microscopy (FE-SEM) images are taken on a ultrahigh resolution scanning electron microscope (JSM-7600F, Japan), operating at an acceleration voltage of 10 kV. The powder X-Ray diffraction (XRD) patterns are recorded on a D/max 2500 VL/PC diffractometer (Japan) equipped with graphite monochromatized Cu Kα radiation (λ = 1.54060 Å). Corresponding work voltage and current are 40 kV and 100 mA, respectively. X-ray photoelectron spectroscopy (XPS) data are acquired on a scanning X-ray microprobe (PHI 5000 Verasa, ULAC-PHI, Inc.) using Al Kα radiation. The binding energies of Mo3d and N1s are calibrated using C1s peak (BE = 284.6 eV) as standard. Raman spectra are obtained on Lab-RAM HR800 with excitation by an argon ion laser (514.5 nm). The Fourier transform infrared (FT-IR) spectra are collected on a Nexus 670 spectrometer. Nitrogen adsorption-desorption measurements are performed at 77 K on a Micromeritics ASAP 2050 system. The samples are degassed overnight at 393 K.

1.5 Electrochemical measurements

Electrochemical tests for three-electrode system. The electrochemical performances are first carried out in a three electrode system with a 0.5 M H_2SO_4 electrolyte solution. The PPy-PMo_{12}/rGO or PPy/rGO modified glassy carbon electrode (the diameter of about 3mm), a platinum wire, and a Ag/AgCl electrode are used as the working electrode, counter electrode and reference electrode, respectively. The cyclic voltammetries (CVs) and galvanostatic charge/discharge tests are performed at 25 °C on a CHI 660D electrochemical workstation (Shanghai, Chenhua Co.).

Fabrication and electrochemical test for PPG-SSCs. First, 80 wt% of PPy-PMo_{12}/rGO, 10 wt% of PTFE and 10 wt% of ATB are homogeneously mixed to obtain a slurry. Then, the slurry is coated on the PET sheets that are deposited with a layer of Au film (~3-5 nm thick). These coated PET sheets are used as a working electrode after drying in a vacuum at 50 °C for 12 h. Subsequently, two slices of such electrodes are immersed in the PVA/H_2SO_4 gel solution for 5 ~ 10 min to adsorb a layer of solid electrolyte. After vaporizing the excess water, two pieces of the electrodes containing the electrolyte are pressed together on a sheeting-out roller. Thus, the stacked PPG-SSCs are fabricated. PPG-SSCs are evaluated for their supercapacitive performance using an Autolab (Netherlands) electrochemical workstation with a two-electrode system. The CVs at different scan rates and bending angles are

recorded at the potential of -0.20 to 0.80 V for the PPy-PMo_{12}/rGO ternary nanohybrids based solid-state devices. The galvanostatic charge-discharge curves are tested at various current densities. The gel electrolyte is prepared as follows: 3 g of H_2SO_4 is added into 30 mL of deionized water, and then 3 g of PVA powder is added. The whole mixture is then heated to 85°C while vigorously stirring until the solution becomes clear.

2. Supplementary characterization

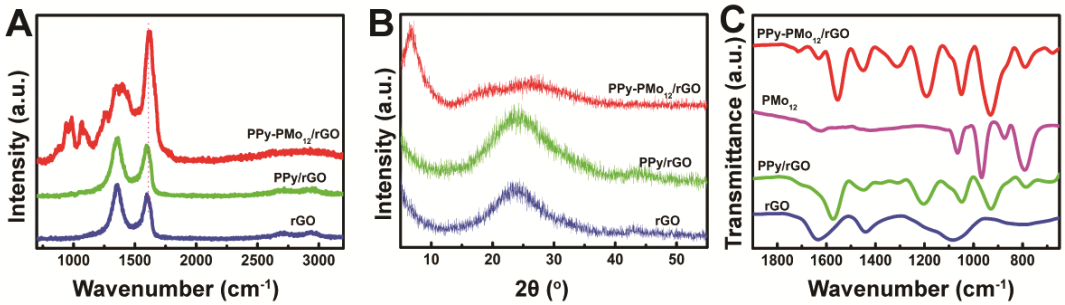

Fig. S1 A) Raman spectra and B) XRD patterns of PPy-PMo_{12}/rGO TNHs, PPy/rGO, and pure rGO, respectively. C) FT-IR spectra of PPy-PMo_{12}/rGO TNHs, PMo_{12}, PPy/rGO, and pure rGO, respectively.

Fig. S1A shows the Raman spectrum of as-synthesized PPy-PMo_{12}/rGO TNHs. For comparison, the Raman spectra of pure rGO and PPy/rGO control samples are also provided. For pure rGO, two characteristic Raman peaks at 1358 and 1598 cm^{-1} are observed, which corresponding to the D (sp^3 C) and G (sp^2 C) bands respectively. Generally, the relative intensity ratio of the D band (I_D) to G band (I_G) is an important parameter for evaluating the degree of graphitization of a specific carbon-based material.[2] The ratio of I_D to I_G is about 1.28 for pure rGO, indicating that some disordered carbons or restored defects result from using hydrazine hydrate to remove several oxygen-containing groups of initial GO.[3] As for PPy/rGO binary composites, the strong D-band peak or slightly reduced ratio of I_D to I_G (~1.27) reveals that their graphitization degree is also low because they still contain a large number of defects.[4] Additionally, no distinct Raman peaks that originate from PPy are observed in PPy/rGO sample, implying that the surfaces of PPy microspheres are covered with or encapsulated by rGO sheets.[5] While for PPy-PMo_{12}/rGO TNHs, an intense G band at around 1588 cm^{-1} is observed in the Raman spectrum, suggesting the presence of a large amount of graphitized C and a decrease of disordered C in this sample. The PPy-PMo_{12}/rGO sample exhibits a series of characteristic Raman peaks for PPy centered at about 931, 976, 1053, 1244, 1371, 1411 and 1588 cm^{-1}.[5] These peaks indicate the successful polymerization of Py by PMo_{12} along the graphene sheets.[6] The related XRD patterns for PPy-PMo_{12}/rGO TNHs, rGO and PPy/rGO are shown in Fig. S1B. The characteristic diffraction peak at 11.2° for GO disappears, and only a diffraction peak centered at about 23.7° that assigned to few-layered stacked graphene, is observed in pure rGO sample.[7,8] Regarding PPy/rGO sample, a very broad diffraction peak centered at about 24.1° is observed, which is slightly shifted toward high angle direction compared with pure rGO due to the presence of planar aromatic pyrrole rings. This result suggests that the rGO sheets are wrapped around PPy microsheets *via* the electrostatic and π–π stacking interactions between them. In contrast to PPy/rGO control sample, the PPy-PMo_{12} /rGO TNHs exhibit a new and sharp diffraction peak below 10° along

with a much broader diffraction peak at around 18 ~ 32° due to the presence of PMo_{12}. Moreover, the FT-IR spectra shown in Fig. S1C further confirm the presence of PPy and PMo_{12} components in obtained TNHs. Compared with rGO, several new peaks that originate from PPy are observed in the spectrum of PPy/rGO sample. The new peaks at 1571 and 1448 cm^{-1} are attributed to C=C and C-N stretching vibrations in the pyrrole ring, respectively. The bands at 1309 and 1203 cm^{-1} are assigned to the C-H in-plane ring-bending modes and the C-N in-plane ring deformation and bending modes, respectively, implying the combination of PPy with rGO sheets.[9-11] Usually, four types of oxygen atomic structures are present in the PMo_{12} unit cell: central oxygen (O_c), terminal oxygen (O_t), bridged oxygen of two octahedral sharing a corner (O_b), and bridged oxygen sharing an edge (O_e). In PPy-PMo_{12}/rGO TNHs, the four observed characteristic bands centered at 1049, 931, 863, 790 cm^{-1} are assigned to the stretching vibrations of P-O_c, Mo=O_t, Mo-O_b-Mo and Mo-O_e-Mo, respectively,[12-14] indicating that the PMo_{12} component with the Keggin ion geometry has been successfully implanted into the final product.

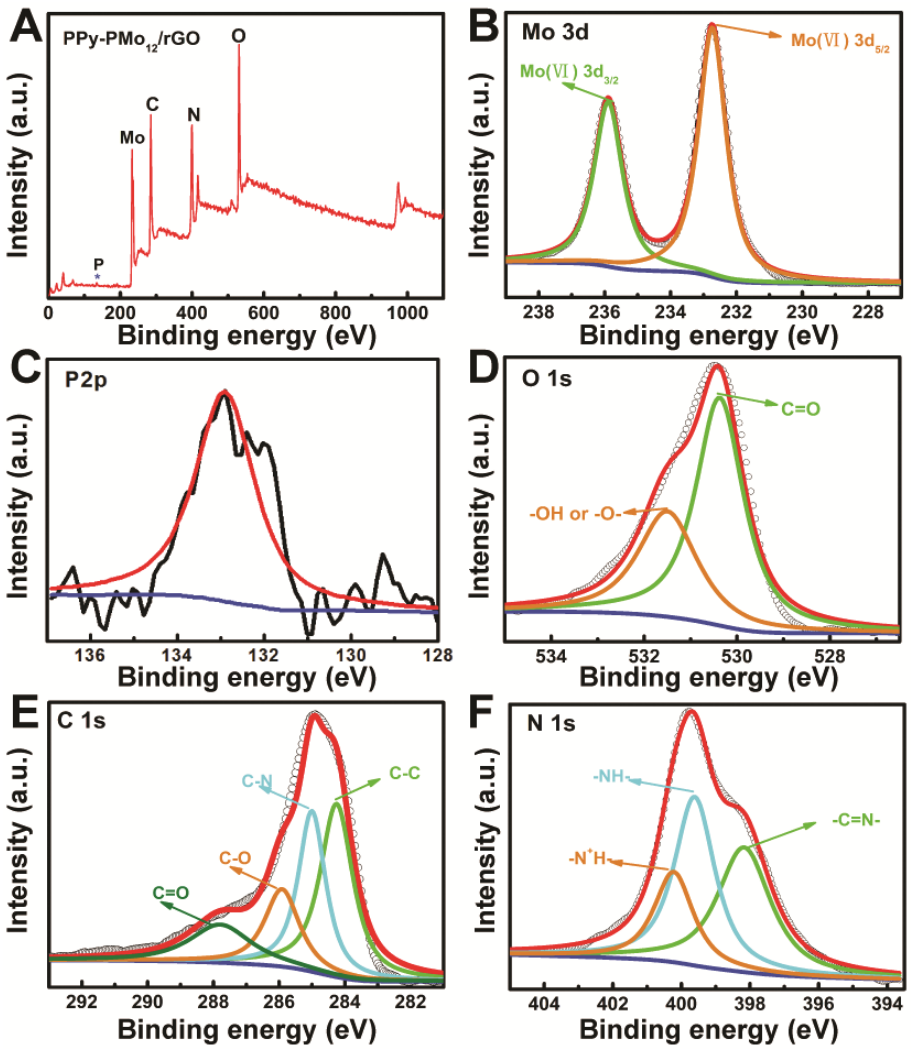

Fig. S2 A) Survey XPS spectrum of the obtained PPy-PMo_{12}/rGO TNHs. B-F) Fine XPS spectrum for (B) Mo 3d, (C) P 2p, (D) O 1s, (E) C 1s and (F) N 1s, respectively.

The composition of PPy-PMo_{12}/rGO TNHs and the valence state of Mo are further examined by XPS. The

survey XPS spectrum (Fig. S2A) exhibits that the main elements present in the TNHs are Mo, P, O, C, and N. The corresponding fine XPS spectrum of Mo 3d (Fig. S2B) reveals that the binding energies of Mo $3d_{5/2}$ and Mo $3d_{3/2}$ are 232.4 and 235.8 eV respectively, indicating that the valence state of Mo in the TNHs is mainly +VI.[15,16] This result is consistent with our initial assumption that the Mo(VI) in PMo_{12} will be reduced to Mo (V) when initiating the polymerization reaction of Py, and subsequently the generated Mo(V) species will be re-oxidized to Mo(VI) by GO or oxygen in air.[17] Combined with the fine XPS spectra of P 2p (Fig. S2C) and O 1s (Fig. S2D), the presence of PMo_{12} in the TNHs can be identified. Fig. S2E shows the fine XPS spectrum of C 1s in obtained TNHs. Compared with the initial GO, the C=O and C-O groups in obtained TNHs greatly decrease or disappear, confirming that the initial GO has been reduced to rGO using our synthetic protocol.[18] By deconvolution of C 1s peak, the binding energy at 285 eV reveals the presence of C-N group in obtained TNHs. The corresponding fine XPS spectrum of N 1s (Fig. S2F) shows that the binding energy of N 1s is about 398.3 eV, implying the existence of pyrrol N in the TNHs. Thus, combining the fine XPS spectra for C 1s and N 1s, the existence of PPy in obtained TNHs can be confirmed.

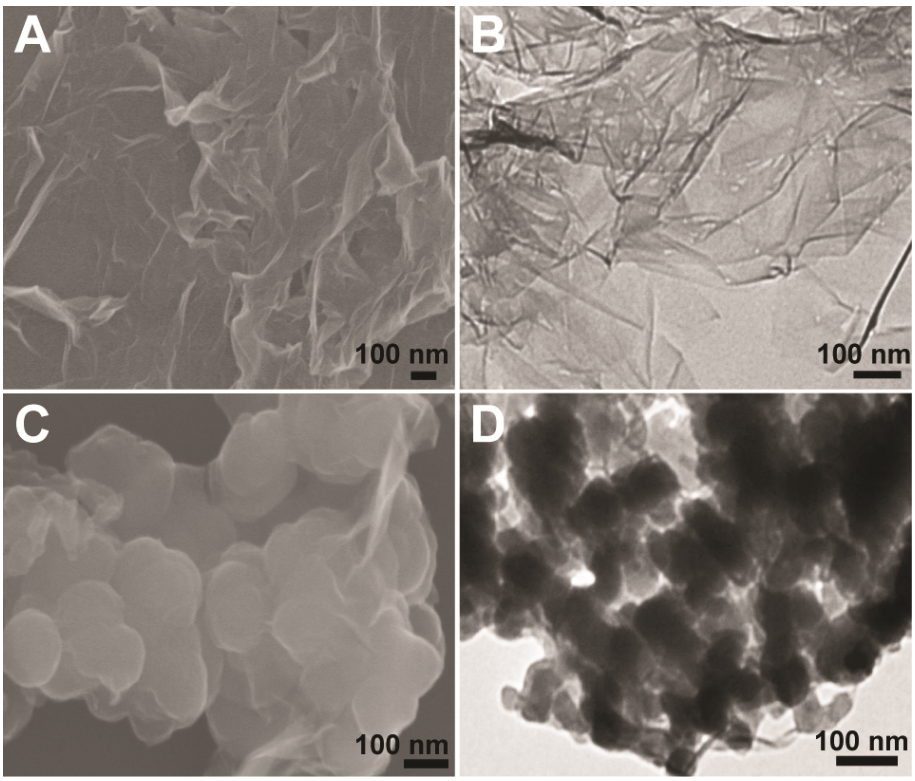

Fig. S3 A) FE-SEM image of pure rGO. B) TEM image of pure rGO. C) FE-SEM image of PPy/rGO binary composites. D) TEM image of PPy/rGO binary composites.

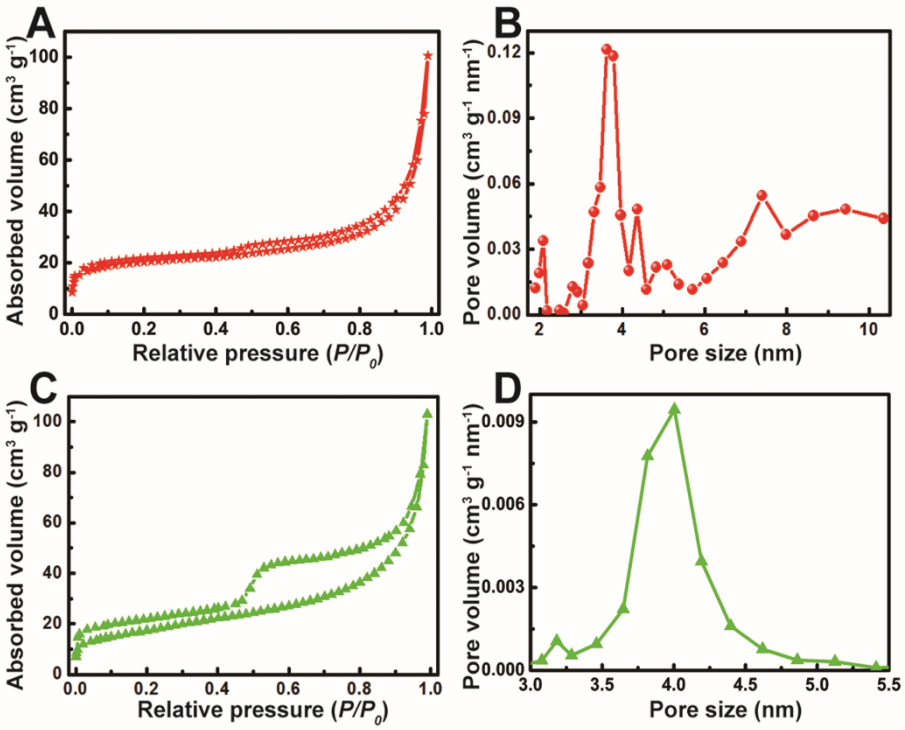

Fig. S4 A) N_2 adsorption-desorption isothermal curve and B) the corresponding pore-size distribution plot for PPy-PMo_{12}/rGO TNHs. C) N_2 adsorption-desorption isothermal curve and D) the related pore-size distribution plot for PPy/rGO control sample.

Fig. S4 shows the N_2 adsorption-desorption isotherm curves and pore size distribution (PSD) plots for PPy-PMo_{12}/rGO TNHs and PPy/rGO control sample. For PPy-PMo_{12}/rGO TNHs, only a small hysteresis loop is observed, indicating that the main pores in the TNHs are mesopores. By contrast, the PPy/rGO control sample shows an obvious and large hysteresis loop, implying the presence of relatively small mesopores. The N_2 adsorption-desorption isotherm plots show that the Brunauer-Emmett-Teller (BET) specific surface area of PPy-PMo_{12}/rGO TNHs is higher than that of PPy/rGO. The corresponding PSD plot verifies that the pore sizes of the TNHs are mainly in the range of 2 ~ 10 nm, resulting from the voids or spaces between the fish scale-like flakes. As respect to PPy/rGO, its average pore size is about 3 ~ 4.5 nm, potentially originating from the re-stacking of rGO sheets. The relatively large pore size of PPy-PMo_{12}/rGO TNHs facilitates intercalation and deintercalation of electrolyte ions, beneficial to improve the performance of fabricated SCs.

3. Electrochemical testing results (three-electrode system)

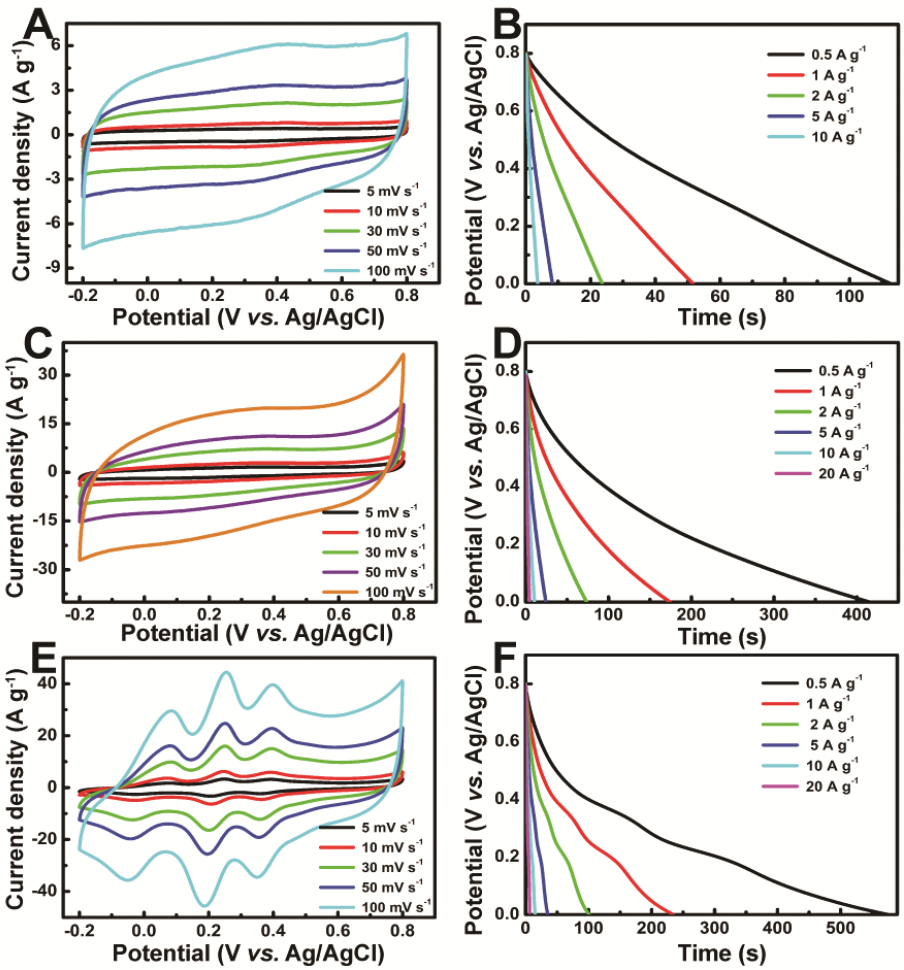

Fig. S5 CV plots measured at different scan rates (A) and galvanostatic discharge branch plots (B) for pure rGO. CV curves measured at different scan rates (C) and galvanostatic discharge branch plots (D) for PPy/rGO. CV plots measured at different scan rates (E) and galvanostatic discharge branch plots (F) for PPy-PMo_{12}/rGO TNHs. The tests are performed in a standard three-electrode system and the used electrolyte is 0.5 M H_2SO_4 solution.

Table S1: Comparison of specific capacitance of PPy-PMo_{12}/rGO TNHs with other reported graphene and POMs based composite materials

Materials	Electrolyte	Current density	Specific capacity	Ref.
Graphene/Mn_3O_4	1 M Na_2SO_4	1 A g^{-1}	115 F g^{-1}	19
graphene/carbon black	gPVAP-H_2SO_4	0.5 A g^{-1}	144.5 F g^{-1}	19
Graphene network	PVA–H_3PO_4	0.1 μA	4.2 mF cm^{-2}	20
graphene/polyaniline/graphene	PVA/H_2SO_4	2 mA cm^{-2}	107 mF cm^{-2}	21
PPy@Nanocellulose@Graphene oxide	2 M NaCl	0.2 A g^{-1}	244 F g^{-1}	22
PPy/GO	2 M NaCl	5 A g^{-1}	48 F g^{-1}	22
Cs-PMo_{12}/CNT	Nafion+1 M H_2SO_4	0.2 A g^{-1}	285 F g^{-1}	23
PMo_{12}–PANI/GS	----	20 mV s^{-1}	363.5 F g^{-1}	14
PPy-PMo_{12}/rGO	0.5 M H_2SO_4	1 A g^{-1}	295 F g^{-1}	this work

4. Bending and flexibility tests of PPG-SSCs device

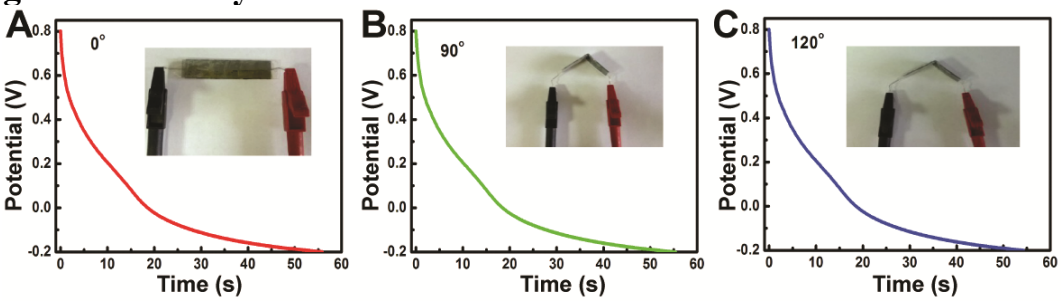

Fig. S6 Flexibility and mechanical stability tests of PPG-SSCs device by recording galvanostatic discharge curves at the bending angles of 0° (A), 90° (B), and 120° (C). The insets show the photographs for each bending tests.

5. Cycling performance evaluation of PPG-SSCs device

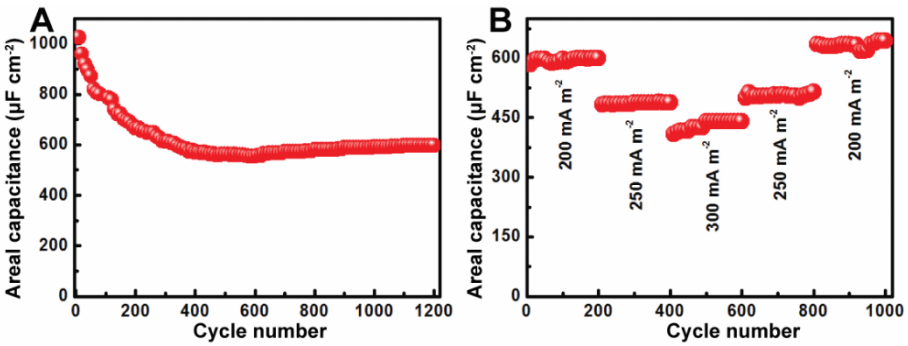

Fig. S7 A) Evaluation of areal capacitances *versus* the number of cycles for PPG-SSCs device at the current density of 200 mA m^{-2}. B) Cycling performance of PPG-SSCs measured by progressively varying the current density.

The cycling stability is another key parameter for determining the application of desired device. Fig. S7A shows the stability curve for PPG-SSCs device at a constant current density of 200 mA m^{-2}. Due to presence of PPy that will suffer the swelling and shrinking during long-term charge/discharge cycles, it is difficult to avoid capacity degradation.[24] After 300 cycles, the PPG-SSCs device shows a decrease in capacitance and 60% of the initial capacitance can be retained. At the following 900 cycles, the device is stable and 98% of capacitance can be maintained relative to the 300th cycle, indicating a good cycling stability of the TNHs electrode. The decrease of capacitance during the first 300 cycles may be attributed to the ineffective contacts between part of unstable PPy spheres and rGO sheets and the subsequent deterioration of the PPy. During the last 900 cycles, excellent stability may result from the rGO, which provides robust support for the PPy-PMo_{12} species and alleviates their swelling and shrinking during cycling tests.[25] The cycling performance of the device is further evaluated by progressively varying the current density (Fig. S7B). After performing 1200 cycles at 200 mA m^{-2} to ensure the device in a steady state, it undergoes cycling tests at different current densities. After cycled at various current densities for 200 continuous cycles and followed by returning to initial current density, the initial capacitance of the device could be recovered and maintained for additional 200 cycles without a noticeable decrease. It is noteworthy that the areal capacitance of the device even increases 7% (from 600 to 644 μF cm^{-2}) at the final 200 cycles compared with the first 200 cycles at 200 mA m^{-2}. These results illustrate that the PPG-SSCs device can meet the requirements of long

lifespan and good rate capabilities, which are important criteria for special energy storage devices.

6. Notes and references

1. J. H. Lee, N. Park, B. G. Kim, D. S. Jung, K. Im, J. Hur and J. W. Choi, *ACS Nano* 2013, **7**, 9366.
2. T. Qian, C. Yu, S. Wu and J. Shen, *J. Mater. Chem. A* 2013, **1**, 6539.
3. Y. Zhou, Q. Bao, L. A. L. Tang, Y. Zhong and K. P. Loh, *Chem. Mater.* 2009, **21**, 2950.
4. L. Qie, W. Chen, H. Xu, X. Xiong, Y. Jiang, F. Zou, X. Hu, Y. Xin, Z. Zhang and Y. Huang, *Energy Environ. Sci.* 2013, **6**, 2497.
5. Y. Zhao, J. Liu, Y. Hu, H. Cheng, C. Hu, C. Jiang, L. Jiang, A. Cao and L. Qu, *Adv. Mater.* **2013**, **25**, 591.
6. J. Wang, Y. Xu, F. Yan, J. Zhu and J. Wang, *J. Power Sources* 2011, **196**, 2373.
7. H. L. Guo, P. Su, X. Kang and S.-K. Ning, *J. Mater. Chem. A* 2013, **1**, 2248.
8. R. Liu, S. Li, X. Yu, G. Zhang, S. Zhang, J. Yao, B. Keita, L. Nadjo and L. Zhi, *Small* 2012, **8**, 1398.
9. X. Zhang, X. Zeng, M. Yang and Y. Qi, *ACS Appl. Mater. Interface* 2014, **6**, 1125.
10. Y. Yang, C. Wang, B. Yue, S. Gambhir, C. O. Too and G. G. Wallace, *Adv. Energy Mater.* 2012, **2**, 266.
11. C. Zhu, J. Zhai, D. Wen and S. Dong, *J. Mater. Chem.* 2012, **22**, 6300.
12. D. Zhou and B. H. Han, *Adv. Funct. Mater.* 2010, **20**, 2717.
13. C. Rocchiccioli-Deltcheff, M. Fournier, R. Franck and R. Thouvenot, *Inorg. Chem.* 1983, **22**, 207.
14. Z. Cui, C. X. Guo, W. Yuan and C. M. Li, *Phys. Chem. Chem. Phys.* 2012, **14**, 12823.
15. A. Dolbecq, J. D. Compain, P. Mialane, J. Marrot, F. Secheresse, B. Keita, L. R. Holzle, F. Miserque and L. Nadjo, *Chem. Eur. J* 2009, **15**, 733.
16. Y. Zhu, Z. Yuan, W. Cui, Z. Wu, Q. Sun, S. Wang, Z. Kang and B. Sun, *J. Mater. Chem. A* 2014, **2**, 1436.
17. P. Gómez-Romero and M. Lira-Cantú, *Adv. Mater.* 1997, **9**, 144.
18. Y. Meng, K. Wang, Y. Zhang and Z. Wei, *Adv. Mater.* 2013, **25**, 6985.
19. H. Fei, C. Yang, H. Bao and G. Wang, *J. Power Sources*, 2014, **266**, 488.
20. X. Fan, T. Chen and L. Dai, *RSC Adv*., 2014, **4**, 36996.
21. F. Xiao, S. Yang, Z. Zhang, H. Liu, J. Xiao, L. Wan, J. Luo, S. Wang and Y. Liu, *Sci Rep*, 2015, **5**, 9359.
22. Z. Wang, P. Tammela, M. Stromme and L. Nyholm, *Nanoscale*, 2015, **7**, 3418.
23. A. K. Cuentas-Gallegos, R. Martínez-Rosales, M. Baibarac, P. Gómez-Romero and M. E. Rincón, *Electrochem. Commun*., 2007, **9**, 2088.
24. K. Wang, H. Wu, Y. Meng and Z. Wei, *Small* 2014, **10**,14.
25. Q. Wu, Y. Xu, Z. Yao, A. Liu and G. Shi, *ACS Nano* 2010, **4**,1963.

